Available online at www.sciencedirect.com
SCIENCE DIRECT®
Journal of Sound and Vibration 281 (2005) 965–993
JOURNAL OF SOUND AND VIBRATION
www.elsevier.com/locate/jsvi

Super- and sub-harmonic response calculations for a torsional system with clearance nonlinearity using the harmonic balance method

T.C. Kim, T.E. Rook, R. Singh*

Acoustics and Dynamics Laboratory, Department of Mechanical Engineering and The Center for Automotive Research, The Ohio State University, 650 Ackerman Road, Columbus, OH 43210-1107, USA

Received 17 October 2002; accepted 10 February 2004
Available online 13 October 2004

Abstract

This article presents a new multi-term harmonic balance method (HBM) for nonlinear frequency response calculations of a torsional sub-system containing a clearance type nonlinearity. The ability of the simplified subsystem to capture the salient behavior of the larger system is verified by the comparison of results to experimental data. Unlike previous analytical and numerical methods, the proposed HBM includes adaptive arc-length continuation and stability calculation capabilities to find periodic solutions in multi-valued nonlinear frequency response regimes as well as to improve convergence. Essential steps of the proposed HBM calculations are introduced, and it is validated by comparing time and frequency domain predictions with those yielded by numerical solutions, experimental studies, or analog simulations for several examples. Then, nonlinear frequency response characteristics of an oscillator with clearance nonlinearity are examined with focus on super- and sub-harmonics. We also explore some issues that are not fully resolved in the literature. For instance, the effect of mean operating point is examined for $\alpha = 0$ and $\alpha = 0.18 - 0.25$ cases where α is the stiffness ratio of the piecewise-linear elastic function. In addition, the number of harmonic terms that must be included in the HBM response calculations, given sinusoidal excitation, has been investigated. Finally, some simple analytical predictions for super and sub-harmonic resonances are presented.

*Corresponding author. Tel.: +1-614-292-9044; fax: +1-614-292-3163.
E-mail address: singh.3@osu.edu (R. Singh).

0022-460X/$ - see front matter © 2004 Elsevier Ltd. All rights reserved.
doi:10.1016/j.jsv.2004.02.039

Nomenclature

a	Fourier transformed relative displacement δ
b	stage transition point (rad)
c	Fourier component of non-linear function in HBM
C	viscous damping coefficient (Nm s)
F	effective external torque (Nm/kg m^2)
$f()$	nonlinear function (rad)
I	effective torsional moment of inertia (kg m^2)
I_i	torsional moment of inertia (kg m^2)
J	Jacobian matrix
K	torsional stiffness (Nm/rad)
ℓ	separation between primary harmonic and mean operating point
n	harmonic index
N	sampling points per cycle in HBM
q	sub-harmonic index
Q	input vector
r	residual in time domain
R	residual in frequency domain
t	time (s)
T	torque (Nm)
α	stiffness ratio
δ, $\dot{\delta}$, $\ddot{\delta}$	relative displacement, velocity and acceleration (rad, rad/s, rad/s^2)
ε	perturbation part of $\delta(t)$
Γ	DFT matrix
φ	phase (rad)
Λ	gearbox temperature
λ	natural frequency (rad/s)
θ, $\dot{\theta}$, $\ddot{\theta}$	absolute displacement, velocity and acceleration (rad, rad/s, rad/s^2)
ϑ	scaled time ($\vartheta = \omega t$)
τ	period (s)
Ω	non-dimensional frequency ($\Omega = \omega_p/\omega_r$)
$\overline{\Omega}_{P1}$	non-dimensional primary harmonic of compliant stiffness
ω	angular velocity or continuation parameter (rad/s)
Ξ	derivative of DFT matrix
ψ	time toward transition points (s)
$\Im$	Fourier transform

Subscripts

$-$	column vector form
$=$	matrix form
1,2,3...	stiffness or damping stages; element index
D	drag damping
e	external excitation
f	friction related term
h	clutch hub-spline related
j	torque harmonic index
m	mean component
max	maximum limit
min	minimum limit
p	alternating or perturbation component
r	resonance
rms	root-mean-square value
S	stiffness related term
s	periodic term
V	viscous damping related term

Superscripts

$\cdot$, $\cdot\cdot$	first and second derivative with respect to time
$-$	non-dimensional value
$+$	pseudo inverse of matrix
$*$	periodic solution part
$\sim$	augmented vector
T	transpose of matrix
-1	inverse of matrix

Abbreviations

AS	analog-computer Simulation
DFT	discrete Fourier Transform
HBM	harmonic Balance Method
LTI	linear Time-Invariant
MDOF	multi-Degree of Freedom
NS	numerical Simulation (Runge–Kutta 4(5))

NSU	numerical Simulation with Up Frequency Sweep	SDOF	single Degree of Freedom
NSD	numerical Simulation with Down Frequency Sweep	QR	QR-decomposition algorithm

1. Introduction

1.1. Clearance nonlinearity

Vehicle drivetrains and other torsional systems often contain multi-staged clutches, gear pairs with backlashes, splines with clearances, dual-mass flywheels with one or two stages and the like [1–21]. One could view such practical systems in terms of coupled torsional sub-systems, each one containing one clearance type nonlinearity given by function $f(\delta,\dot{\delta})$, where δ and $\dot{\delta}$ are the relative displacement and velocity, respectively, as shown in Fig. 1(a) via a two-degree-of-freedom (2dof) semi-definite torsional system. Although practical devices exhibit dry frictional hysteresis or Hertzian impact damping, we will consider only viscous (subscript V) and fluid induced drag (subscript D) damping elements in this article. The semi-definite system of Fig. 1(a) can be reduced to an equivalent single-degree-of-freedom system (sdof) as shown in Fig. 1(b). The nonlinear function $f(\delta,\dot{\delta})$ may be decomposed into stiffness (f_S) and damping (f_V) characteristics. In particular, the stiffness function (f_S in rad) is related to torque $T_S = Kf_S(\delta)$ (in Nm), where $\delta = \theta_1 - \theta_2$ (in rad), and K is the second stage stiffness (in Nm/rad). Fig. 2(a) shows $f_S(\delta)$ where α and 1 represent the linear stiffness of the first and second stages. The transition is assumed to take place at $\pm b$ in a symmetric manner. Note that α is the stiffness ratio of stiffnesses, can be viewed as a measure of the severity of piecewise linear system. Mathematically, $f_S(\delta)$ is as follows:

$$f_S(\delta) = \begin{cases} \delta - (1-\alpha)b, & b < \delta, \\ \alpha\delta, & -b \leqslant \delta \leqslant b, \\ \delta + (1-\alpha)b, & \delta < -b, \end{cases}$$
$$= \delta + (1-\alpha)\,\frac{|\delta - b| - |\delta + b|}{2}. \tag{1}$$

Further, the term $|\delta - b|$ can be written as in terms of sign or signum function that could be smoothened and regularized [17–21]:

$$|\delta - b| = (\delta - b)\mathrm{sgn}(\delta - b). \tag{2}$$

For the viscous damping element, the damping torque T_V is given by $Cf_V(\dot{\delta}) = C\dot{\delta}$ where C is the damping coefficient in Nm s/rad. Note that the units of $f_V(\dot{\delta})$ are in angular velocity, rad/s. When $\alpha = 1, f_S(\delta) = \delta$ and $f_S(\delta)$ becomes a linear function. When α is very close to unity (but less than 1) the component may be viewed as weakly nonlinear. It would exhibit stiffening type

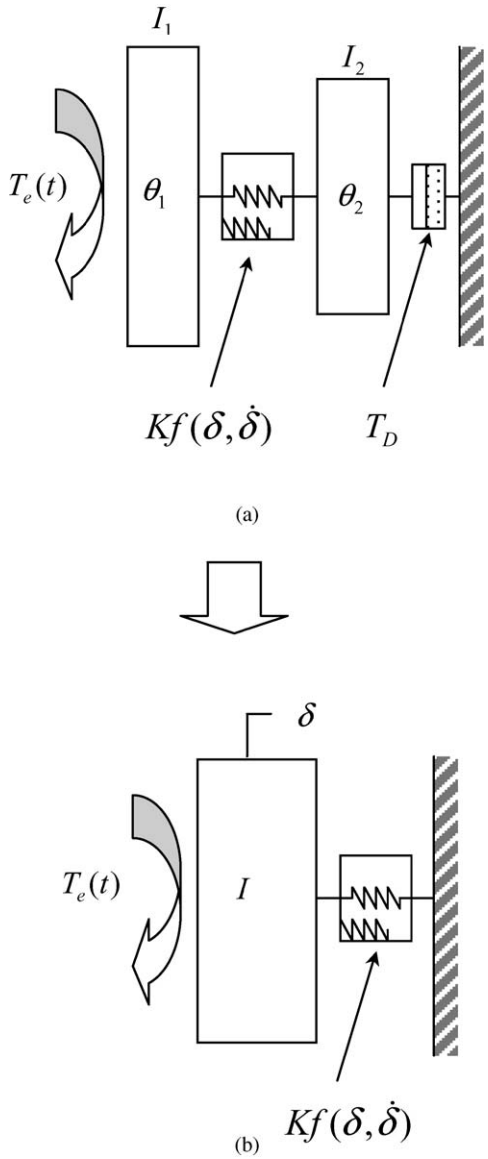

Fig. 1. Torsional sub-system with clearance nonlinearity. (a) 2dof semi-definite system; (b) sdof definite system.

nonlinearity from the first stage stiffness. In contrast, when $\alpha > 1$, the stiffness saturation type nonlinearity is demonstrated. In the case of a multi-staged torsional clutch damper, α is usually from 0.0 to 0.5, and it could be classified as a strong nonlinearity [5–9,11,13–14]. In this paper, the particular cases of $0.10 < \alpha < 0.25$ for a clutch or $\alpha = 0$ for a gear pair with backlash are studied. Even after taking account of the lubrication oil film between the mating teeth, the first stage stiffness of $\alpha \ll 0$ (within the gear backlash) is still negligible. Such a condition ($0.0 \leqslant \alpha \leqslant 0.25$) can

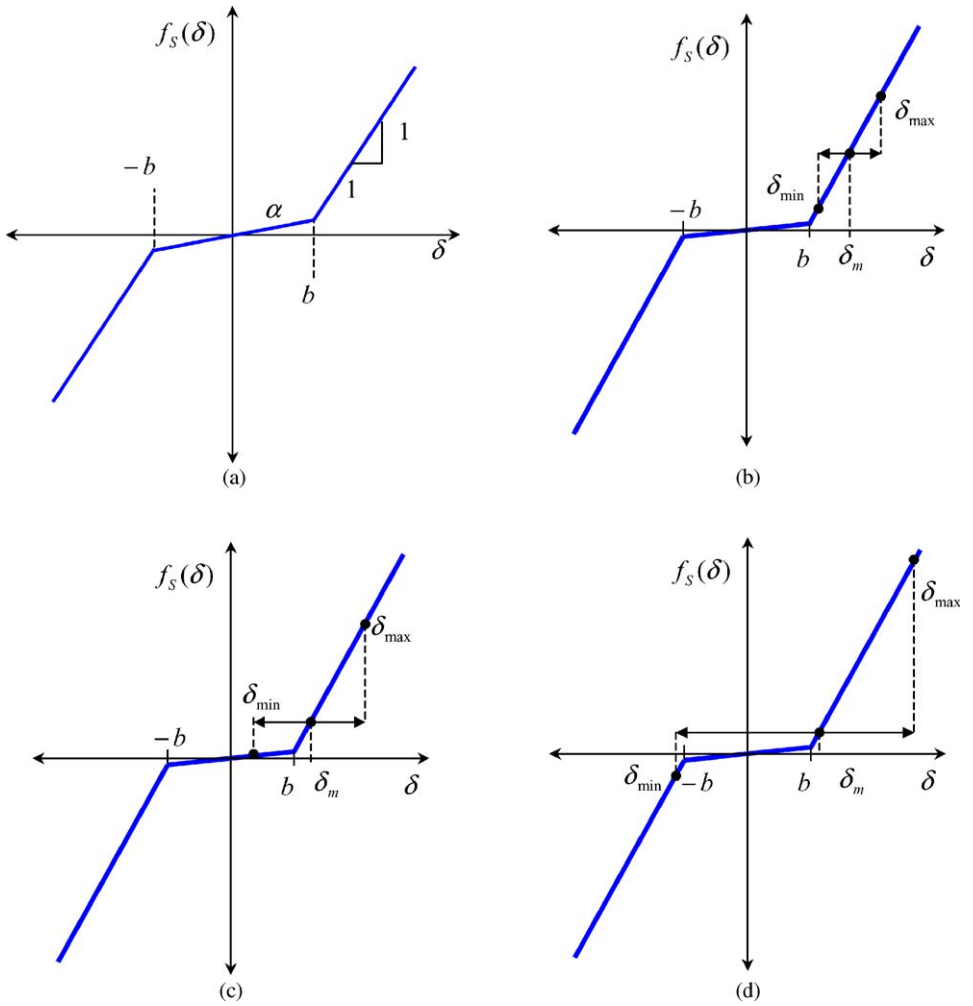

Fig. 2. Clearance nonlinearity function $f_S(\delta)$ and illustration of impact cases. δ_m will be in the second-stage stiffness regime if $F_m > \alpha b$. Therefore, $\delta_m = F_m/\alpha$ when δ_m is in the 1st stage, and $\delta_m = F_m + (1-\alpha)b$ when δ_m is in the 2nd stage. (a) $f_S(\delta)$; (b) no impact; (c) single-sided impact; (d) double-sided impact.

be categorized as an extremely strong nonlinearity and is therefore of primary interest in our study. A unique feature of this case is that the mean operating point (δ_m) always starts from the second-stage of the stiffness due to the presence of a mean load (F_m) as shown in Fig. 2. Therefore, the three possible impact conditions (no impact, single-sided impact, and double-sided impact) where δ_m starts from the second-stage stiffness, need to be fully considered. However, for the case where δ_m migrates to the first stage, both single- and double-sided impacts from the first stage stiffness should be examined as well. The operating conditions and impact regimes related to the moderate nonlinearity ($\alpha > 0.25$) will be explained in a subsequent paper that will also examines friction-induced hysteresis damping.

1.2. Frequency response calculations

Clearance type nonlinearities within torsional systems, such as those shown in Figs. 1 and 2, have been investigated using a variety of techniques [1–21], including analog [5,8,11,12,18,21] and digital simulations [7,14–17,19–21]. However, some of these analyses have placed emphasis on determination of the actual time-domain histories given harmonic excitations, neglecting detailed parametric studies because they require intensive computational resources. Additionally, the resulting time-domain motion can be very complicated and may include super-harmonic and sub-harmonic resonances [4–6,15,18] or even exhibit quasi-periodic chaotic behavior [2,4,10,12,15]. Determining these behaviors using standard numerical integration method is rather difficult since the entire map of initial conditions must be simulated. When multiple clearance nonlinearities are coupled, understanding the system behavior becomes further complicated. Thus, clearly a need exists for the development of specialized semi-analytical techniques that can overcome the deficiencies of simple methods. An example of such specialized methods would be any of the techniques used to solve periodic boundary condition problems (e.g. shooting and harmonic balance) rather than initial condition problems with their associated lengthy transients. Furthermore, from the dynamic design point of view, the steady-state frequency response function of the system (whether full or reduced) is useful (refer to previous researches [5–8,16,18,26]). However, the concept of such a function is more complicated for the nonlinear case, even experimentally because of the following issues: the loss of linear superposition, multi-frequency response for a single-frequency excitation, jump phenomenon, multi-valued solutions, and the possibility of aperiodic solutions [4–7]. Nonetheless, some investigators have calculated frequency response characteristics, but it has been mostly limited to a narrow frequency range well below resonance [2,4,5,10] or at resonance [22,23].

The current work is a direct extension of the previous describing function analysis that was introduced by Comparin and Singh [4–7]. It will also extend the work of Padmanabhan and Singh [17,18] and Rook and Singh [16,17] who investigated both time and frequency domain characteristics of clearance nonlinearities based on the application of harmonic balance. We propose a new harmonic balance method (HBM) and then apply it to determine super- and sub-harmonic response solutions given a single harmonic excitation. In addition, arc-length continuation with adaptive frequency step-size, and stability indicators are tested in the HBM code. Results are compared with those obtained using numerical (digital) simulations based on the modified Runge–Kutta 5(4) integration technique due to Dormand and Prince [24], which has been found to be reliable by Padmanabhan and others [17,18,20]. Finally, influences of sub- and super-harmonic responses are discussed in detail.

2. Problem formulation

2.1. Scope

The excitation torque $T_e(t)$, from an internal combustion engine, fluctuates significantly between low (around the compression stage) and high (around the ignition stage) values. Therefore, the $T_e(t)$ can be decomposed into mean T_m and perturbation $T_p(t)$ parts. The

fundamental frequency ω_p of $T_p(t)$ depends on type of the engine, number of cylinders and crankshaft configuration. For example, the four-stroke engine with V-6, 120° crankshaft configuration fires three times within a crank revolution. Therefore, the firing frequency ω_p is $3\omega_e$ where ω_e represents the crankshaft rotational speed. Similarly, for an I-4 engine, $\omega_p = 2\omega_e$. Express $T_e(t)$ via Fourier series as

$$T_e(t) = T_m + \sum_{j=1}^{\infty} T_{pj} \sin(j\omega_p t + \varphi_j) \quad \text{or} \quad T_e(t) = T_m + \sum_{j=1}^{\infty} T_{pj} \cos(j\omega_p t + \varphi_j). \tag{3}$$

Here, j represents the torque harmonic index. The mean term is $T_m = E\left[\tilde{T}_e(t)\right]$ where $E[\,]$ is the expectation operator. Under no power condition, it should be equal to the drag torque $T_D(\omega_e, \Lambda)$ generated within the transmission where Λ is the gearbox temperature [19]. Therefore, the coupled nonlinear second-order differential equations for the sub-system of Fig. 1(a) are

$$I_1\ddot{\theta}_1 + C(\dot{\theta}_1 - \dot{\theta}_2) + Kf(\theta_1 - \theta_2, \dot{\theta}_1 - \dot{\theta}_2) = T_e(t), \tag{4a}$$

$$I_2\ddot{\theta}_2 - C(\dot{\theta}_1 - \dot{\theta}_2) - Kf(\theta_1 - \theta_2, \dot{\theta}_1 - \dot{\theta}_2) = -T_D(t). \tag{4b}$$

Here, θ_1 and θ_2 are absolute angular displacements, C is the viscous damping coefficient, and K is the linear torsional stiffness corresponding to the second stage in Fig. 2(a). After an application of the initial conditions, $\ddot{\theta}_1(0) = \ddot{\theta}_2(0) = 0$, and $\theta_2(0) = 0$, the relationship between T_D and T_m is written as $T_D = T_m$. In geared transmission problems, one has motion fluctuations superimposed upon the mean rotation of the shafts and gears. The non-stationary gross rotations are of importance in understanding how the engine power is transmitted through the gearing to the wheels, but for studying noise and vibration scenarios they are of less interest. Rather it is the stationary fluctuating rotations which contribute to noise and vibration issues. The transmission system is mathematically semi-definite in order to admit the gross (i.e. rigid-body) rotations, but these rigid-body motions are unnecessary to understand our problem and in fact create undesirable numerical issues (e.g. drift of absolute rotation to very large values). Therefore, it becomes attractive to eliminate the rigid-body motions in the simulation and that has the added benefit of reducing the order of the system by 1 dof (i.e. the rigid-body mode). Ref. [4,6,16–21] show the utilization of a condensation such as implemented herein. The aforementioned coupled equations for the semi-definite system can be reduced to a single equation for the equivalent sdof system of Fig. 1(b) where $\delta = \theta_1 - \theta_2$.

$$\ddot{\delta} + \frac{C}{I}\dot{\delta} + \frac{K}{I}f(\delta, \dot{\delta}) = F(t) = F_m + \sum_{j=1}^{\infty} F_{pj} \sin(j\omega_p t + \varphi_j). \tag{5}$$

Here, $I = I_1 I_2/(I_1 + I_2)$ is the effective torsional inertia, $F_m = T_m/I$ is the effective mean torque, and $F_{pj} = T_{pj}/I_1$ is the effective amplitude for the jth harmonic of pulsating torque. The validity of this reduced model will be explored in Section 4.

2.2. Objectives

The first major objective of this article is to propose a new multi-term HBM with parametric contribution and an adaptive frequency step control capability. The proposed technique is

capable of finding both stable and unstable multi-valued solutions given a harmonic excitation. The HBM is validated by comparing time or frequency domain predictions with those yielded by analog simulations (as described by Comparin and Singh in Refs. [5–7]) and digital simulations. The validity of a reduced order model is also confirmed against experimental studies (as reported in Refs. [17–18,20]). The second major objective is to examine the nonlinear frequency response functions of the clearance type nonlinear system of Figs. 1 and 2. In particular, we focus attention on super- and sub-harmonics and explore some issues that were not fully resolved by Comparin and Singh [5–7]. For instance, the effect of mean operating point (δ_m) is examined for $\alpha = 0$ and $\alpha \ll 1.0$ cases. In addition, the number of harmonic terms ($n_{\max}$) that must be included in HBM will be examined. Finally, some simple analytical prediction for super- and sub-harmonic resonances will be presented.

3. Proposed multi-term harmonic balance method

The HBM is essentially a form of the Galerkin's method of residual minimization [25–27]. The residual or error $r(t)$ is the gap between true input and estimated solutions, and it should go to zero for a $\delta(t)$ that satisfies the nonlinear differential equation. In time-domain analysis, the residual should be zero for all time spans, and this is called the *strong* form. From Eq. (5), before normalization by the inertia term I the equation of motion becomes

$$I\ddot{\delta} + C\dot{\delta} + Kf(\delta, \dot{\delta}) = T(t) = T_m + \sum_{j=1}^{j_{\max}} T_{pj} \sin(j\omega_p t + \varphi_j). \tag{6}$$

In this article, the excitation is assumed to be a single harmonic ($j_{\max} = 1$). However, the steady-state response is assumed to be a certain multiple of harmonics (n) of the fundamental frequency ω_p:

$$\delta(t) = \delta_m + \sum_{n=1}^{n_{\max}} \delta_{pn} \sin(n\omega_p t + \varphi_n). \tag{7}$$

The number of term ($n_{\max}$) of 12 is used in this study, although fewer harmonics could be sufficient in some cases. Also, we will simulate sub-harmonic responses given a pure harmonic input assuming the fundamental response period ($\tau_p = 2\pi/\omega_p$) to be equal to $q\tau_p = ((2\pi/q)\omega_p)$, where, q is the sub-harmonic index, $\omega = \omega_p = 2\pi/\tau_p$, and τ_p is the fundamental period of response and excitation. Multi-term harmonic input cases will be investigated in future article.

The *strong* form residual is defined as

$$r(t) = T(t) - I\ddot{\delta} - C\dot{\delta} - Kf(\delta, \dot{\delta}) \to 0 \quad \forall t. \tag{8}$$

When the input and response characteristics of a nonlinear system are periodic, frequency-domain analysis can be applied by introducing the Fourier transformation ($\Im$) of both sides. The Eq. (9) shows the result after the Fourier transformation of equation (8) that yields the *weak* form residual (i.e. satisfied in only a least-squares sense):

$$\Im(r(t)) = \Im(T(t)) - I\Im(\ddot{\delta}) - C\Im(\dot{\delta}) - K\Im(f(\delta, \dot{\delta})) \to 0 \quad \forall t. \tag{9}$$

Let the Fourier component vector of the sampled output be vector $\underline{a} = \Im(\delta(t))$, then the minimization of the residual in Newton–Raphson form is expressed as

$$\underline{R} \cong \underline{R}_0 + \frac{\partial \underline{R}}{\partial \underline{a}} \Delta \underline{a}. \tag{10}$$

Here, $\underline{R}_0$ is the residual from an initial guess, and the correction factor is defined as $\Delta \underline{a} = -\left(\partial \underline{R} / \partial \underline{a}\right)^{-1} \underline{R}$. Finding the solution $\underline{a}$ is an iterative process, and the Newton–Raphson method is used for this process. The term $\partial \underline{R} / \partial \underline{a}$ is the Jacobian matrix $\underline{\underline{J}}$ used in the Newton–Raphson corrector. The Fourier transformation of a periodic output after nonlinearities can be written as below. Similarly, $q\omega_p$ is used instead of ω for the qth sub-harmonic analysis.

$$\Im(\delta(t)) \Rightarrow \begin{Bmatrix} \delta(t_0) \\ \delta(t_1) \\ \vdots \\ \delta(t_{N-2}) \\ \delta(t_{N-1}) \end{Bmatrix} = \begin{bmatrix} 1 & \sin(\omega t_0) & \cos(\omega t_0) & \sin(2\omega t_0) & \cdots \\ 1 & \sin(\omega t_1) & \cos(\omega t_1) & \sin(2\omega t_1) & \cdots \\ \vdots & \vdots & \vdots & \vdots & \vdots \\ 1 & \sin(\omega t_{N-2}) & \cos(\omega t_{N-2}) & \sin(2\omega t_{N-2}) & \cdots \\ 1 & \sin(\omega t_{N-1}) & \cos(\omega t_{N-1}) & \sin(2\omega t_{N-1}) & \cdots \end{bmatrix} \begin{Bmatrix} a_0 \\ a_1 \\ \vdots \\ a_{2n_{\max}} \\ a_{2n_{\max}+1} \end{Bmatrix} = \underline{\underline{\Gamma}}\,\underline{a}. \tag{11}$$

Here, the vector $\delta(t_i)$ is the output signal from the nonlinear function. For example, it is the relative displacement in time domain across the nonlinearity. Since we assumed the output to be periodic, the vector $\delta(t_i)$ is periodic. As noted in Fig. 3, $\delta(t_0)$ is the point where a period starts, and $\delta(t_{N-1})$ is one step Δt before the period τ_p ends. The symbol N denotes the number of sampling points or resolution within cycle τ_p.

The column vector $\underline{a}$ contains amplitudes of each Fourier component approximated by the discrete fourier transformation (DFT) process. The number of sampling points N should be equal to or larger than the desired number of terms $(2n_{\max}+1)$ as shown in Eq. (6) since one must

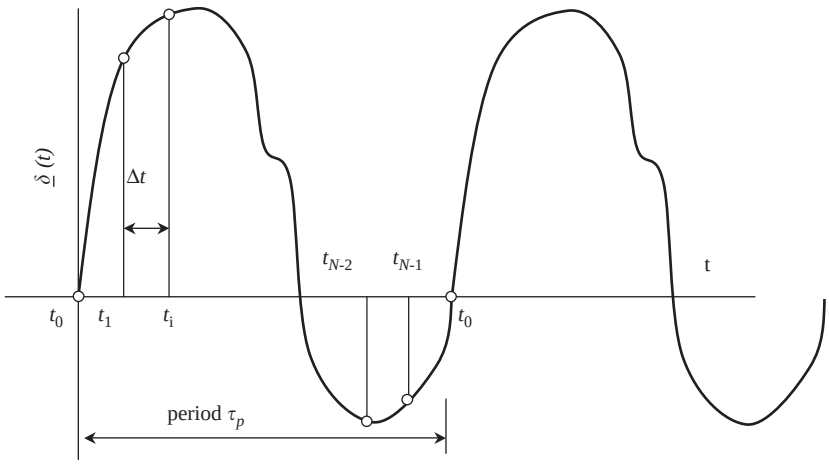

Fig. 3. Sampling of nonlinear response $\underline{\delta}(t)$ for Fourier approximation. Here, $i = 0, \ldots, N-1$.

consider the mean term along with magnitude and phase of chosen harmonics. Therefore, the derivative of the time series can be constructed by differentiating each member in the DFT matrix or multiplying it by the derivative matrix $\underline{\underline{\Xi}}$, defined as $\Im(\dot{\delta}(t)) \Rightarrow \underline{\dot{\delta}} = \underline{\underline{\Gamma}}\,\underline{\underline{\Xi}}\,\underline{a}$. In the same manner, the spectral acceleration vector is $\Im(\ddot{\delta}(t)) \Rightarrow \underline{\ddot{\delta}} = \underline{\underline{\Gamma}}\,\underline{\underline{\Xi}}^2\,\underline{a}$. By defining the time scaling of $\vartheta = \omega t$ with $\vartheta \in [0, 2\pi)$ and $\dot{\delta} = \mathrm{d}\delta/\mathrm{d}t = \omega/\omega\,\mathrm{d}\delta/\mathrm{d}t = \omega \mathrm{d}\delta/\mathrm{d}\vartheta = \omega\delta'$, the recalculation of the DFT matrices for each frequency can be avoided in the Newton–Raphson type HBM algorithm. In other words, the DFT matrices are defined only once in the beginning of the calculation program as below and stored (or cached) for subsequent calculations. Accordingly, we obtain

$$\underline{\underline{\Gamma}} = \begin{bmatrix} 1 & \sin(\vartheta_0) & \cos(\vartheta_0) & \sin(\vartheta_0) & \cdots \\ 1 & \sin(\vartheta_1) & \cos(\vartheta_1) & \sin(\vartheta_1) & \cdots \\ \vdots & \vdots & \vdots & \vdots & \vdots \\ 1 & \sin(\vartheta_{n-1}) & \cos(\vartheta_{n-1}) & \sin(\vartheta_{n-1}) & \cdots \\ 1 & \sin(\vartheta_n) & \cos(\vartheta_n) & \sin(\vartheta_n) & \cdots \end{bmatrix}, \tag{12a}$$

$$\underline{\underline{\Xi}} = \omega \begin{bmatrix} 0 & & & & \\ & \begin{bmatrix} 1 & 0 \\ 0 & -1 \end{bmatrix} & & & \\ & & \begin{bmatrix} 2 & 0 \\ 0 & -2 \end{bmatrix} & & \\ & & & \ddots & \end{bmatrix}, \tag{12b}$$

$$\underline{\underline{\Xi}} = -\omega^2 \mathrm{diag}\left[0, 1^2, 1^2, 2^2, ..., n^2, n^2\right]. \tag{12c}$$

The Fourier transform of the known input is

$$\Im(T_e(t)) \Rightarrow \underline{T_e}(t) = \underline{\underline{\Gamma}}\,\underline{Q}. \tag{13}$$

The vector $\underline{Q}$ can be defined as $\underline{Q} = \underline{\underline{\Gamma}}^+\,\underline{T_e}(t)$, and the components of $\underline{Q}$ are the amplitudes of each harmonic in torque excitation. Here, matrix $\underline{\underline{\Gamma}}^+$ is the pseudo-inverse of the DFT matrix defined as $\underline{\underline{\Gamma}}^+ = (\underline{\underline{\Gamma}}^T\,\underline{\underline{\Gamma}})^{-1}\underline{\underline{\Gamma}}^{\mathrm{T}}$. Again, the $\underline{\underline{\Gamma}}^+\,\underline{T_e} = \underline{Q}$ needs to be calculated only once because $\underline{Q}$ is the excitation vector in frequency domain. In the same manner, the column vector $\underline{c}$, the Fourier components of the nonlinear function, is defined

$$\underline{c} = \underline{\underline{\Gamma}}^+\,\underline{f} \quad \text{where } \underline{f} = \Im[f(\delta, \dot{\delta})]. \tag{14}$$

Therefore, the residual in the frequency domain using the Fourier approximation is rewritten as below, and this should go to zero.

$$\underline{\underline{\Gamma}}\,\underline{R} = \underline{\underline{\Gamma}}\,\underline{\underline{\Gamma}}^+ T_e - \underline{I}\,\underline{\underline{\Gamma}}\,\underline{\underline{\Xi}}^2\,\underline{a} - \underline{\underline{C}}\,\underline{\underline{\Gamma}}\,\underline{\underline{\Xi}}^1\,\underline{a} - \underline{\underline{K}}\,\underline{\underline{\Gamma}}\,\underline{\underline{\Xi}}^0\,\underline{c} \to 0, \tag{15}$$

$$\underline{R} = \underline{Q} - \underline{I}\,\underline{\underline{\Xi}}^2 - \underline{\underline{C}}\,\underline{\underline{\Xi}}^1 - \underline{\underline{K}}\,\underline{\underline{\Xi}}^0\,\underline{c} \to 0. \tag{16}$$

Now, the Jacobian $\underline{\underline{J}}$ for the system, which is required for the Newton–Raphson technique, is written as

$$\underline{\underline{J}} = \frac{\partial \underline{R}}{\partial \underline{a}} = -\underline{\underline{I}}\,\underline{\underline{\Xi}}^2 - \underline{\underline{C}}\,\underline{\underline{\Xi}}^1 - \underline{\underline{K}}\frac{\partial \underline{c}}{\partial \underline{a}}. \tag{17}$$

The term $\partial \underline{c}/\partial \underline{a}$ is difficult to calculate directly. Therefore, some authors have used the finite difference approximation [28–31]. Instead, we propose to calculate the partial derivative of the nonlinearity in the time domain and convert it to the frequency domain. As defined before, $\underline{c} = \underline{\underline{\Gamma}}^+ \underline{f}$ and $\underline{a} = \underline{\underline{\Gamma}}^+ \underline{\delta}$. Therefore,

$$\underline{\delta} = \underline{\underline{\Gamma}}\,\underline{a} \rightarrow \frac{\partial \underline{\delta}}{\partial \underline{a}} = \underline{\underline{\Gamma}}. \tag{18}$$

Now, rewrite the term $\partial \underline{c}/\partial \underline{a}$ as

$$\frac{\partial \underline{c}}{\partial \underline{a}} = \frac{\partial(\underline{\underline{\Gamma}}^+ \underline{f})}{\partial \underline{a}} = \underline{\underline{\Gamma}}^+ \frac{\partial \underline{f}}{\partial \underline{a}} = \underline{\underline{\Gamma}}^+ \frac{\partial \underline{f}}{\partial \underline{\delta}} \frac{\partial \underline{\delta}}{\partial \underline{a}} = \underline{\underline{\Gamma}}^+ \frac{\partial \underline{f}}{\partial \underline{\delta}} \underline{\underline{\Gamma}}, \tag{19}$$

where

$$\frac{\partial \underline{f}}{\partial \underline{\delta}} = \mathrm{diag}\left(\frac{\partial f}{\partial \delta}(t_0) \quad \frac{\partial f}{\partial \delta}(t_1) \quad \cdots \quad \frac{\partial f}{\partial \delta}(t_{N-2}) \quad \frac{\partial f}{\partial \delta}(t_{N-1}) \right). \tag{20}$$

The correction amount for the Newton–Raphson is $\Delta \underline{a}^{(k)} = -\underline{\underline{J}}^+ \underline{R}$. The predicted solution is corrected by the equation

$$\underline{a}^{(k+1)} = \underline{a}^{(k)} + \Delta \underline{a}^{(k)}, \tag{21}$$

where the symbol k represents the iteration index. The modified solutions after some iteration should yield closer values to the real solution. The error criteria are defined as

$$||\Delta \underline{a}|| < \varepsilon \ \text{ or } \ ||\underline{R}|| < \varepsilon. \tag{22}$$

When performing frequency sweeps of nonlinear systems, the proper tangent (derivative) calculation is important, though it is somewhat forgiving. Success of the nonlinear calculation is also highly dependent on the proper initial choice of arc-length which may adapt itself throughout the frequency sweep through an arc-length continuation scheme [25,27,28,32]. In our algorithms, the directional decisions in the Newton–Raphson solution scheme are essentially automatic; the use of augmented Jacobian (i.e. adding the column $\partial \underline{R}(\omega)/\partial\omega$ to the matrix $\partial \underline{R}(\delta)/\partial \underline{a}$) and then using the orthogonal–triangular decomposition algorithm (QR) decomposes the space into normal and tangent sub-spaces. The normal direction gives the Newton–corrections during convergence while the tangent gives the direction for the predictor. The key of the arc-length continuation lies in augmenting the space (harmonic coefficients) with the frequency ω, as $\tilde{\underline{a}} = \lfloor \underline{a} \ \ \omega \rfloor^{\mathrm{T}}$ where T is the transpose. Here, ω is the excitation frequency over the range of frequency-domain analysis. From Eq. (16), the augmented residual in frequency domain can be written as [26,33,34]

$$\underline{R}(\underline{a}, \omega) = 0, \tag{23}$$

where ω is no longer always the "independent" variable. The Taylor expansion (10) can be written as

$$\begin{bmatrix} \Delta a \\ \Delta\omega \end{bmatrix} = \begin{bmatrix} \partial \underline{R} & \partial \underline{R} \\ \overline{\partial \underline{a}} & \overline{\partial\omega} \end{bmatrix}^{+} [\underline{R}(\underline{a}, \omega)], \tag{24}$$

where the decomposition of the non-square Jacobian is done via the QR algorithm. As a result, the system is broken down such that the arc-length (tangent) is the independent variable and the normal directions are the dependent. Note that the arc-length is composed of the harmonic coefficients, $\underline{a}$, and the frequency, ω, so that any combination of the variables can be the "independent" variable as necessary. For example, when the frequency response curve approaches a turning point, the "independent" variable gradually switches from frequency to a combination of the harmonic coefficients. In this manner, the algorithm adjusts automatically and smoothly transitions around the turning points. Refinement of the arc-length can be related to both numbers of iterations before convergence and changes in tangential angles of the frequency response function, and greatly improves the convergence of the algorithm. However, HBM with a variable arc-length does not automatically indicate whether a particular solution is stable. Stability in the time-domain is usually determined by the Floquet multipliers [25,27–32]. However, in the frequency domain HBM analysis, stability could be calculated by using a modified algorithm such as Hill's method; this procedure is well explained in Refs. [26,33,34].

Stability analyses provide vital information to the user whether the solution branch followed has passed a turning or bifurcation point and whether the stability has changed. Nevertheless, the stability issues in HBM with arc-length continuation are mostly ignored by previous researchers and often numerical integration is used to analyze this matter. At little extra computational cost, stability can be analyzed in the frequency domain in HBM by adapting Hill's method. This method transforms a linear time-variant system into an eigenvalue problem of a linear-time-invariant (LTI) system [26,33,34]. If we extend the same approach to the nonlinear system Eq. (6) with nonlinear function $f(\delta)$, investigation on the effect of a perturbation around a periodic solution can provide stability information by redefining $\delta(t) = \delta^*(t) + \varepsilon(t)$. Here, $\delta^*(t)$ is a periodic solution and $\varepsilon(t)$ is the perturbation, where $\varepsilon(t)$ consists of a decay term $e^{\lambda t}$ and a periodic term $s(t)$. Therefore, Eq. (9) can be rewritten after substituting $\delta(t) = \delta^{*(t)+\varepsilon(t)=\delta^*(t)+e\lambda t} s(t)$ as

$$I\ddot{\delta}^* + C\dot{\delta}^* + Kf(\delta^*) - T(t) + I\ddot{\varepsilon} + C\dot{\varepsilon} + K\frac{\partial f}{\partial \delta}(\delta^*)\varepsilon = 0. \tag{25}$$

Here, the part $I\ddot{\delta}^* + C\dot{\delta}^* + Kf(\delta^*) - T(t) = 0$ since it is the converged solution to the differential equation. Now, the perturbation part must fulfill the following condition in order to satisfy Eq. (25):

$$I\ddot{\varepsilon} + C\dot{\varepsilon} + K\frac{\partial f}{\partial \delta}(\delta^*)\varepsilon = 0. \tag{26}$$

Eq. (26) is the so-called variational equation [26,34]. Substitute $\varepsilon = (s)e^{\lambda t}$, $\dot{\varepsilon} = (\dot{s} + \lambda s)e^{\lambda t}$, and $\ddot{\varepsilon} = \left(\ddot{s} + 2\lambda\dot{s} + \lambda^2 s\right)e^{\lambda t}$ into Eq. (26) and collect terms of λ, and then factor out $e^{\lambda t}$. Lastly,

application of the Fourier transformation provides us the frequency-domain equation

$$\lambda^2[I\underline{\underline{\Xi}}^0]\,\underline{a}+\lambda^1[2(I\underline{\underline{\Xi}}^1)+(C\underline{\underline{\Xi}}^0)]\,\underline{a}+\lambda^0[I\underline{\underline{\Xi}}^2+C\underline{\underline{\Xi}}^1+K\frac{\partial\,\underline{c}}{\partial\,\underline{a}}]\,\underline{a}=\underline{0}. \tag{27}$$

Here, the term $I\underline{\underline{\Xi}}^2+C\underline{\underline{\Xi}}^1+K\partial\,\underline{c}\,/\partial\,\underline{a}=\underline{J}$, and it is already available from the solution process using Newton–Raphson. From the polynomial eigenvalue solution of Eq. (27), a set of λ_i with real and imaginary parts is found. When the real part of one of the λ_i is positive, this determines that the periodic solution $\delta^*(t)$ is unstable, and this could be used to find the possible bifurcation point.

4. Feasibility study of multi-term harmonic balance method

In order to demonstrate the validity of HBM, an experimental system as shown in Fig. 4(a) is selected [17,18]. This system incorporates two kinds of nonlinearities, the dynamic clutch with stick-slip Coulomb-type friction as well as spline–hub with backlash. When the spline is welded to the clutch hub, its backlash goes to zero and it becomes a linear torsional spring (with shaft stiffness k_S). This process can eliminate the influence of the spline nonlinearity, and only clutch nonlinearity can be examined. Now, the system can be simplified as a sdof sub-system as shown in Fig. 4(b), that is comparable to Fig. 1(b) by the simplification process explained earlier. Since the available experimental result is in terms of $\ddot{\theta}_3$ we develop two simulation models. First, we perform both numerical (NS) and HBM analyses using the multi-degree-of-freedom (mdof) model of Fig. 4(a). Before the simplification, the lumped parameter modeling of this system requires 3dof, and the values of the inertias are listed in Table 1. An additional dummy inertia I_4 is set as $\frac{1}{1000}$ of the smallest physical inertia value only for the HBM calculations; this is required to represent the bi-linear friction within the clutch for the same system. Second, we simplify the above model further and eliminate the friction effect in HBM. This approach can avoid the use of a dummy inertia and now it exactly represents the system of Fig. 1(b). For the dynamic model of the clutch described in Fig. 4(a), k_d is the clutch diaphragm stiffness and k_{c1} is the clutch spring stiffness. The function T_f is the static friction force (torque) that needs to be overcome before slipping is initiated. No assumption is made regarding the time for which the friction damper (given by spring k_d and the friction interface) is stuck or slipping. This is kept track of, in the numerical integration routine, by monitoring the zero crossing of the relative velocity between the friction interface and inertia I_1. The numerical integration routine is also modified to detect the points of sticking to slipping and vice-versa. The excitation torque amplitude (T_p) are adjusted until the displacement (θ_1) magnitude matches that seen in experiment. Both absolute and relative displacements and velocities corresponding to other inertias are calculated by using a mdof numerical simulation that employs the Runge–Kutta 5(4th) order integration scheme. Then, $\ddot{\theta}_1$ calculated from the numerical simulation is fed into the HBM as a reference to extract absolute accelerations, because the HBM is based on the relative term (δ) calculations. Fig. 5(a) shows the measured acceleration ($\ddot{\theta}_3$) time history of the third inertia I_3 for the case without hub-spline backlash. Fig. 5(b) shows simulation results using NS, mdof HBM (with friction), and sdof HBM (without friction). Both NS and mdof HBM show high-frequency influence from the input shaft stiffness and a slight transition from the stick-slip phenomena as well. Yet, the sdof HBM still predicts experimental results very well. As

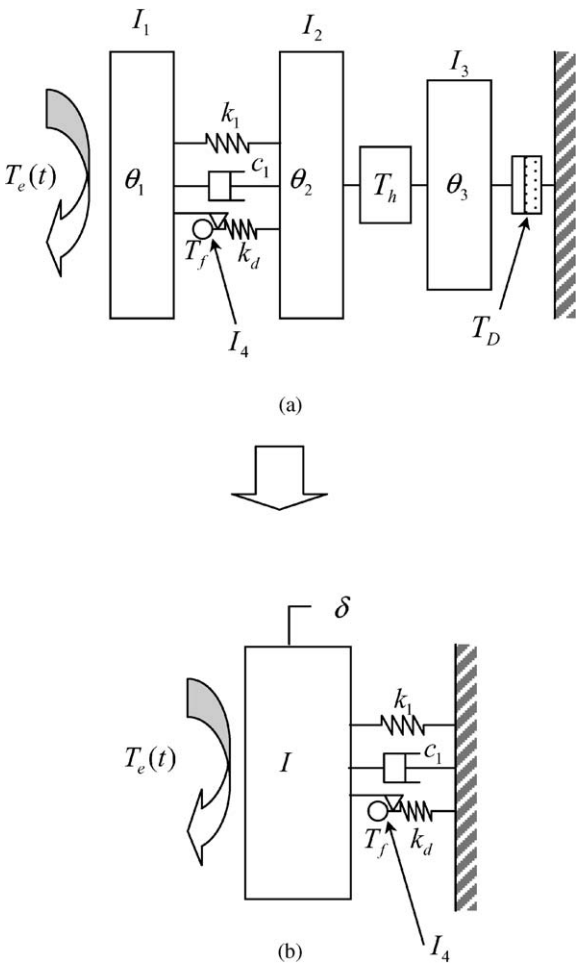

Fig. 4. An experimental torsional system [3–7]. (a) 3dof semi-definite system; (b) sdof definite system. Assume that the spline–hub interface (T_h) is linear, and is very stiff. A dummy inertia (I_4) is used only in HBM calculation.

Table 1
Values used for simulating the system of Fig. 4

Parameters and excitation	Value
Inertias (kg m^2)	$I_1 = 3.43\text{e}{-03}$, $I_2 = 1.37\text{e}{-04}$, $I_3 = 2.0\text{e}{-03}$, $I_4 = I_2/1000$ (only for HBM)
Stiffness (Nm/rad)	$k_{c1} = 250.0$ ($\alpha = 0.167$), $k_{c2} = 1500.0$, $k_d = 6000.0$, $k_s = 19600.0$
Backlash or stiffness transition	$2b = 1.489^\circ$
Excitation	$T_m = 0.2$ (Nm), $T_p = 1.1$ (Nm), $\omega_p = 15.0$ (Hz), $\omega_1 = 45.8$ (Hz)

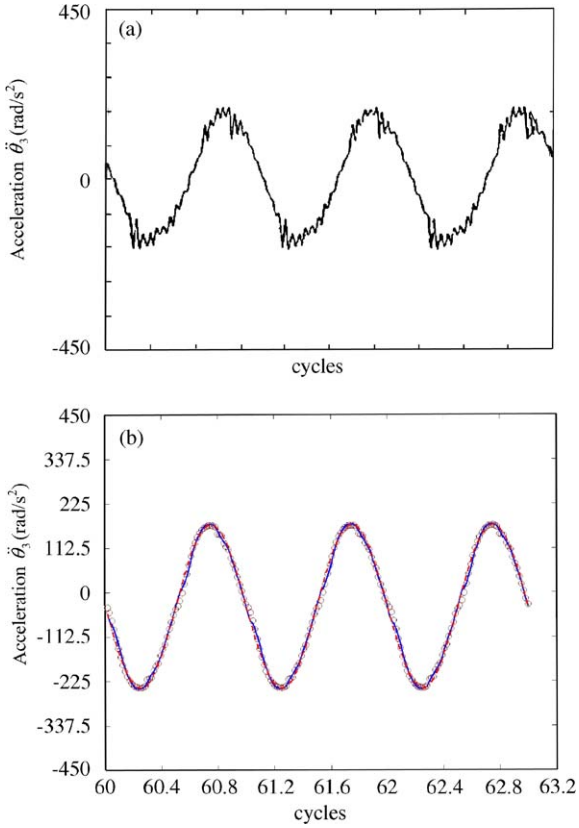

Fig. 5. Comparison of the time-domain results for the system of Fig. 4. (a) Experimental result, (b) simulation results. Key: ○, NS; –, HBM (with friction); – · , HBM (without friction).

seen in Table 2, experimental and simulation results from both NS and HBM match precisely in peak-to-peak amplitudes. The calculation times are however different. The required calculation time in HBM is only 38 s using a Pentium III 400 MHz machine. It is $\frac{1}{4}$ of the calculation time required for the NS case. After a close examination of response curves in the time domain, it is found that both simulation schemes yield virtually the same time signatures as the experiment even in the nonlinear stiffness transition regimes. The reason for small deviations could be because the values of dynamic clutch characteristics (T_f, k_{c1}, and k_d) are estimated. Also, our model ignores the high-frequency oscillations shown in measured acceleration. For the validation purposes, only the dynamic clutch nonlinearity is considered in this paper, and a detailed discussion of mdof HBM and interactions between the two nonlinearities of Fig. 4(b) will be the subject of a subsequent article. From the above results, one may conclude that the reduced model still captures the salient behavior of the actual system, and furthermore that the reduced model lends itself well to simulation via the HBM.

Using the parameters for Cases 1 and 2 of Table 3, the HBM code is studied further. Fig. 6 clearly shows single-sided impacts of Fig. 2(b). The maximum ($\delta_{\max}$), mean (δ_m), and minimum ($\delta_{\min}$) displacement plots can help us in keeping track of the impact conditions. In Fig. 6, possible impacts are seen in δ_m or $\delta_{\min}$ plots. In contrast, the root-mean-square (rms) value of the

Table 2
Comparison between methods for the system of Fig. 4(b)

	Experiment	Numerical integration (NS)	Harmonic balance method (HBM)
$\left\|\ddot{\theta}_3\right\|$ (rad/s^2), p–p	382	389	390
Computation time (t)	—	144 s	38 s

Table 3
Numerical values of various sub-systems

Case	Impact case	Parameters	
		$K = 1.0,\ I = 1.0,\ C = 0.05$	
1	Single-sided	$F_m = 0.050,\ F_{p1} = 0.008,\ b = 10^\circ$	$\alpha = 0.00;\ 0.10;\ 0.25$
2	Double-sided	$F_m = 0.050,\ F_{p1} = 0.030,\ b = 10^\circ$	$\alpha = 0.00;\ 0.10;\ 0.25$

displacement signifies the deviation of multi-term harmonic solutions from the pure sinusoidal results. When the periodic solutions include many harmonics, the deviation gets larger, but when one of the harmonics is dominant, the deviation is smaller. The backbone curve starts at $\overline{\Omega} = 1.0$ where $\overline{\Omega} = \omega_p/\omega_r$ is the dimensionless frequency (speed), ω_p is the excitation frequency (speed) and ω_r is the first natural frequency of the sub-system assuming a linear regime such as the second stage stiffness. Then, the nonlinear frequency curve exhibits softening effects at $\overline{\Omega} = 0.95$ after passing the upper transition point at $b = 0.745$ radian. This softening slope depends on the amount of response δ that resides within the backlash regime ($\alpha = 0$) during a cycle. The comparison shows a close match between numerical simulations (NS) and HBM results in all frequency spans. As seen within the circle "A", both down- (NSD) and up- (NSU) frequency sweeps of numerical simulation (NS) are needed in order to achieve solution points around the nonlinear resonance peak. The NS can solve all stable solutions whether periodic or not, but the entire range of initial conditions should be checked. In addition, the forward numerical integration can only be tried for the stable solution so when it comes to a turning point, it jumps rather than smoothly following the curve, resulting in the jump phenomenon. This limitation can also be observed in some experimental results [11] on a nonlinear gear pair that was excited by the transmission error unlike the torque perturbation we consider in this paper. However, our HBM code with parametric continuation capability can adjust itself for better solution tracking using Newton–Raphson-type solutions, and can provide periodic solutions in multiple valued regimes. A single run of HBM provides all results, even in multi-valued regimes, with the same accuracy as numerical simulation with less than $\frac{1}{4}$ of calculation time. The HBM with only the fundamental harmonic ($n_{\max} = 1$) exhibits significant differences in the primary harmonic resonance peak. The $\delta_{\min}$ from HBM with $n_{\max} = 1$ even shows the double-sided impact. This difference is negligible with a linear stiffness function of $\alpha = 1$, but becomes up to 50% larger when α approaches zero. It can be proven that the influence of higher harmonics in the response becomes more significant for cases when α approaches zero. Fig. 7 clearly shows double-sided impacts of Fig. 2(c). The

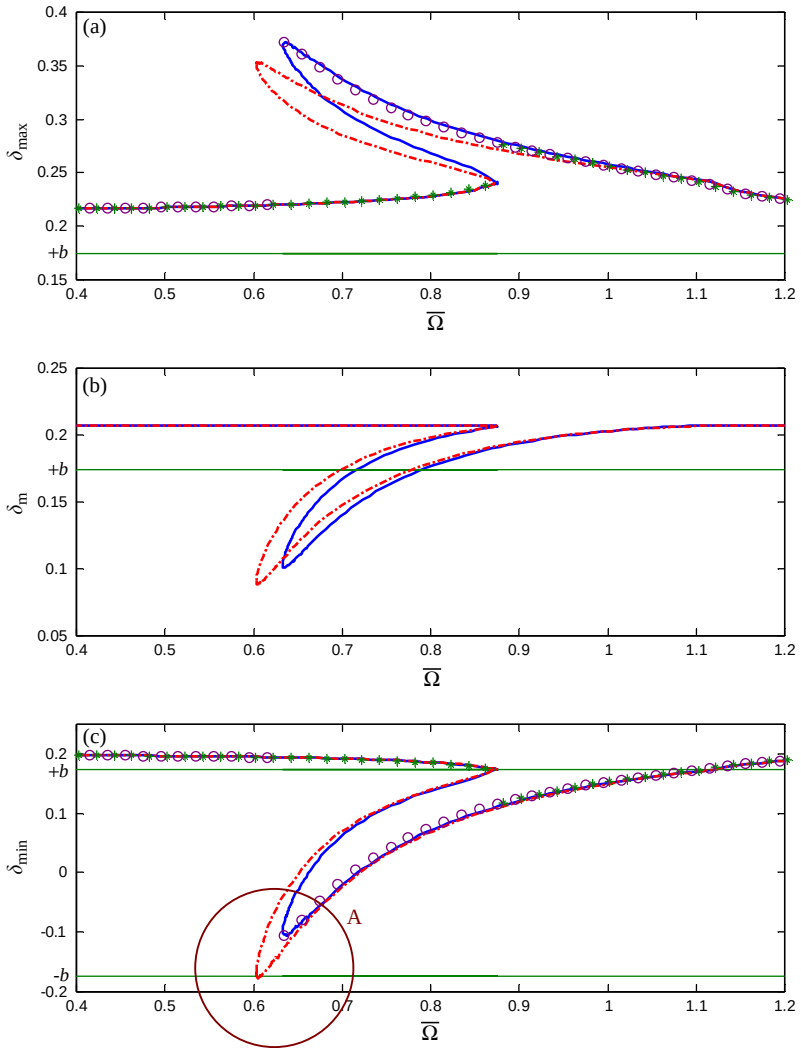

Fig. 6. Comparison between numerical simulation and multi-harmonic HBM for Case 1 of Table 3 when $\alpha = 0.00$. (a) Maximum displacement δ_{max}; (b) mean operating point δ_m; (c) minimum displacement δ_{min}. Key: –, HBM ($n_{max} = 12$); –·, HBM ($n_{max} = 1$); ○, NSD; ∗, NSU.

backbone starts at $\overline{\Omega} = 1.0$ and then saturates to $\overline{\Omega} = 0.82$ after reaching the lower backlash $b = -0.1745$, exhibiting the hardening effect. The HBM results and numerical simulations match with great accuracy for all frequency spans. For the double-sided impact case, HBM (with $n_{max} = 1$) results agree well with those from numerical simulation in peak values at the primary harmonic resonance. However, the mean (δ_m) and maximum (δ_{max}) displacements around the turning point from single-sided impact to double-sided (marked as "B" in Fig. 7) exhibit differences. The minimum number of harmonics (n_{max}) required for reliably simulating the nonlinear frequency response will be discussed in a later section.

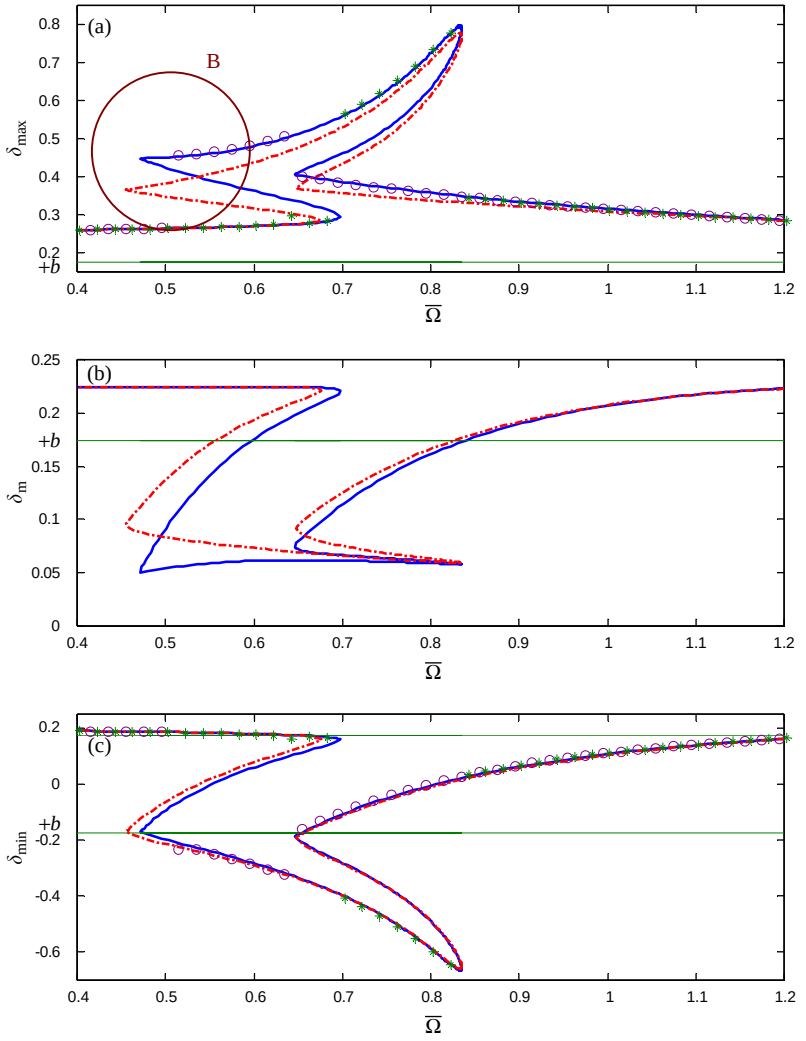

Fig. 7. Comparison between numerical simulation and multi-harmonic HBM for Case 2 of Table 3 when $\alpha = 0.00$. (a) Maximum displacement δ_{max}; (b) mean operating point δ_m; (c) minimum displacement δ_{min}. Key: –, HBM ($n_{max} = 12$); – ·, HBM ($n_{max} = 1$); ○, NSD; ∗, NSU.

5. Typical nonlinear frequency responses

Fig. 8 compares linear and nonlinear frequency responses as calculated by the HBM given Case 2 of Table 3 when $\alpha = 0.25$ for the sub-system of Fig. 1. The nonlinear frequency response is generated by plotting the rms value of $\delta(t)$ vs. $\overline{\Omega}$. Corresponding to a harmonic excitation at ω_p, one would run the numerical simulations (NS) for many ω_p values and then determine the steady-state response over a wide range of $\overline{\Omega}$. In this process we specially calculate the δ_{max} value that may include the effects of sub- or super-harmonics. Conversely, HBM yields the same δ_{rms} values very quickly, unlike the NS.

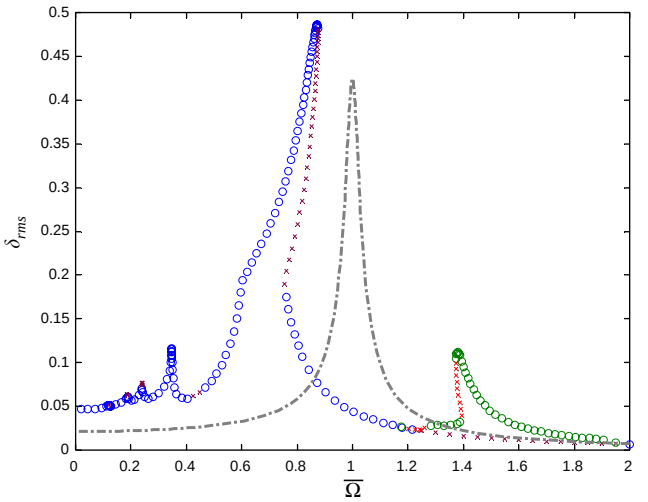

Fig. 8. Linear and nonlinear frequency responses. Key: ○, nonlinear HBM (stable solution); ∗, Nonlinear HBM (unstable solution); – ·, linear analysis.

The nonlinear frequency response of Fig. 8 clearly demonstrates an amplitude-dependent instability leading to severe vibro-impact problems. The fundamental harmonic peak starts from the no-impact case at $\overline{\Omega} = 1.00$ corresponding to the linear system. Then it reduces to $\overline{\Omega} = 0.65$ when undergoing single-sided impacts, and finally saturates to $\overline{\Omega} = 0.80$ for double-sided impacts. In addition, the nonlinear frequency response exhibits several active super-harmonic responses below $\overline{\Omega} = 0.40$, and a sub-harmonic response above $\overline{\Omega} = 1.20$. The linear frequency response curve can not obviously predict these phenomena and their amplitudes are lower than those from the nonlinear analysis, especially below $\overline{\Omega} = 0.9$.

The calculation time required of the HBM analyses including an initial run with τ_p period for primary and super harmonics, and a second run with $2\tau_p$ period for the sub-harmonic peak, requires 350 s when compared with up (NSU) and down (NSD) sinusoidal sweeps in numerical integration (NS) that take at least 3460 s for Case 2 of Table 3 when $\alpha = 0.25$. The reason for significantly high calculation times for the NS is that one must wait longer until the steady state is reached and time steps become finer when the period doubling (sub-harmonics), super-harmonic resonances, quasi-periodic or chaotic responses take place. Since the HBM code is based on the frequency domain calculations, it is not affected by changes in response regimes. Furthermore, the stability indicator in our HBM code (with $n_{\max} = 12$) shows the possible appearances of chaotic or quasi-periodic (“C”), and sub-harmonic (“D”) regimes. As noted in Fig. 9, there is a small regime (“C”) where the HBM and numerical simulation results do not match well. The numerical simulation finds a quasi-periodic regime in Fig. 10(a) with a period doubling cascade that will eventually deteriorate into quasi-periodic or chaotic responses unlike the HBM that assumes to have only the periodic solutions. Yet, another instability occurs in the sub-harmonic regime (“D”). Although sub-harmonic responses are periodic, they are unstable in terms of the assumed τ_p period solution. Re-running the HBM with $q\tau_p$ can simulate the qth sub-harmonic resonances. For instance, the HBM assumes the periodic solution with a period $2\tau_p$ to yield a sub-harmonic

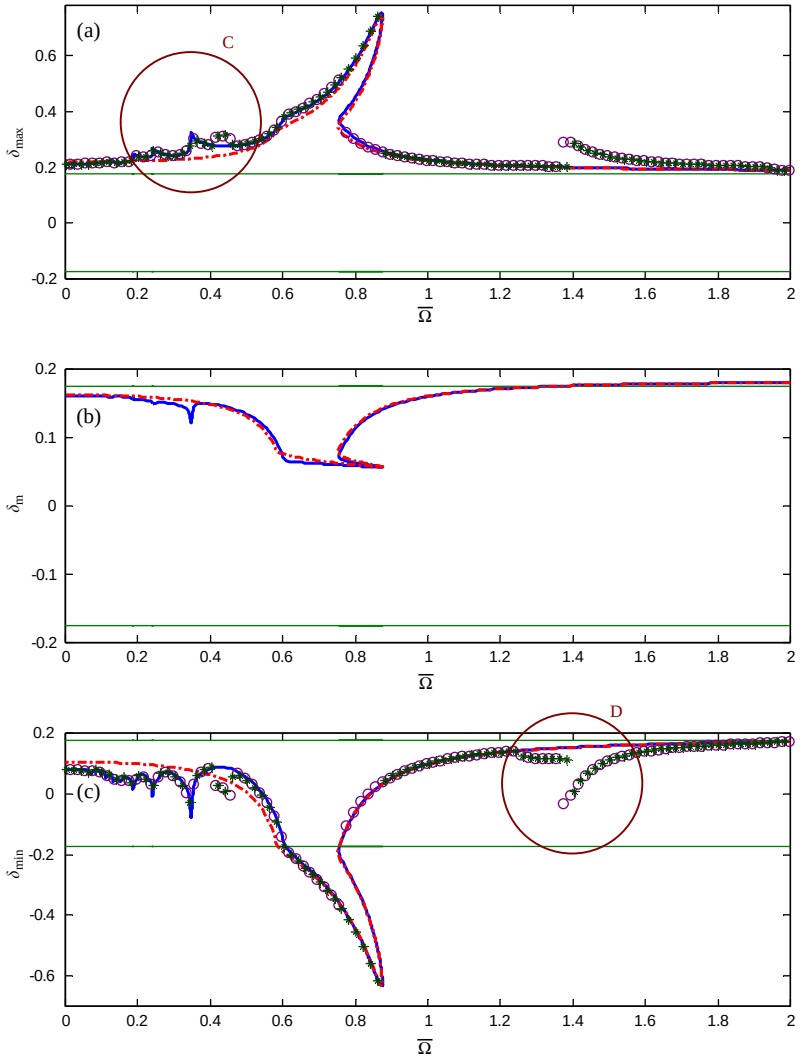

Fig. 9. Effect of the number of harmonics in HBM on response and comparison with numerical simulation. (a) δ_{max}, (b) δ_m, (c) δ_{min}. Key: –, HBM ($n_{max} = 12$); – ·, HBM ($n_{max} = 1$); ○, NSD; ∗, NSU.

peak at $\overline{\Omega} = 1.4$, as evident from the time-domain signature in Fig. 10(b). Numerical simulation and HBM results match exactly since the sub-harmonic response is still periodic.

The effect of the number of harmonics (n_{max}) that could be included in the HBM analysis is clearly visible over the super-harmonic regimes. Fig. 9 shows the difference between $n_{max} =$ 1 and 12 response curves. A very active super-harmonic regime is observed, and the magnitude difference between $n_{max} = 1$ and 12 approaches around 10 to 15 dB over $0.0 < \overline{\Omega} < 0.5$. Further, neither even nor odd harmonics are dominant for a clearance type nonlinearity in contrast with the strictly odd harmonic dominance seen in the Duffing type nonlinearity. As seen in Fig. 11, all of the higher harmonics play an active role in the super-harmonic regime ($0.0 < \overline{\Omega} < 0.5$), and yet the number of super-harmonic peaks that could be calculated by the HBM code depend strictly

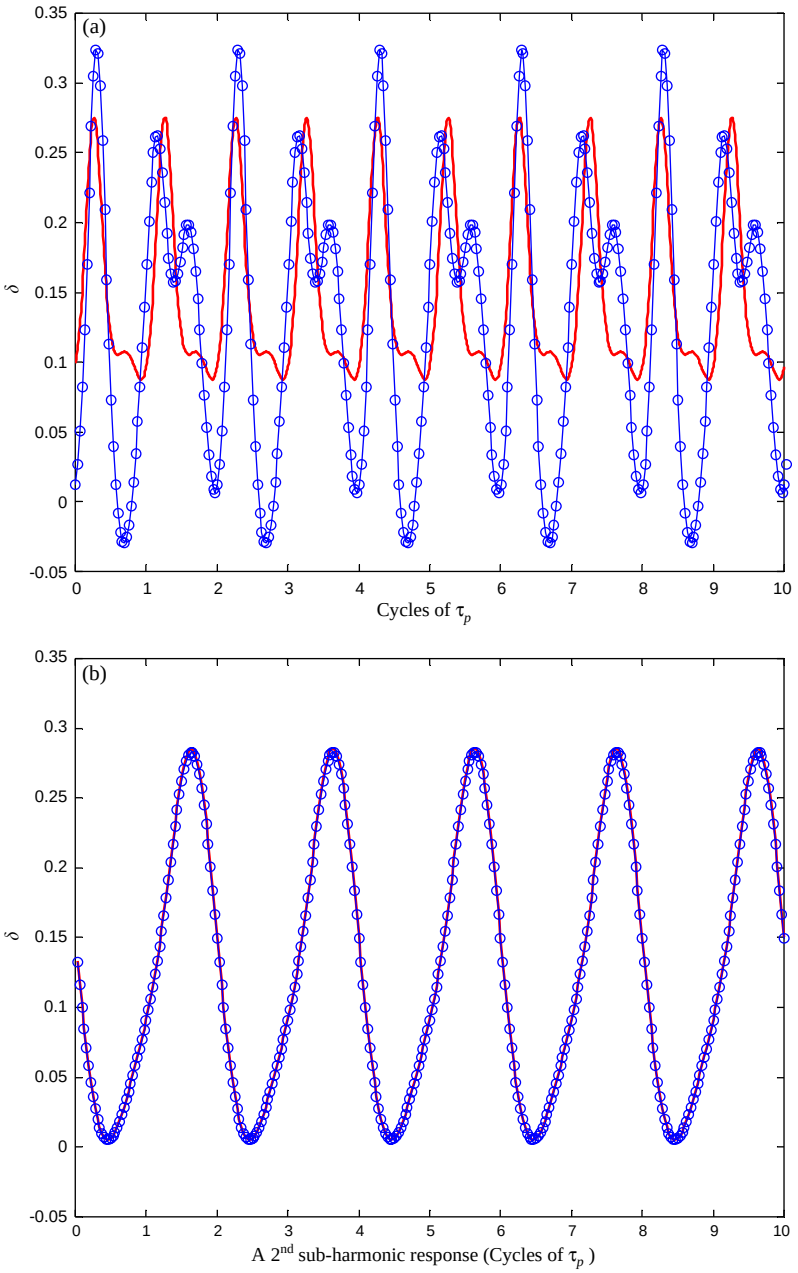

Fig. 10. Time history comparisons for two particular responses. (a) Quasi-periodic response ("C" at $\overline{\Omega} = 0.44$); (b) sub-harmonic response ("D" at $\overline{\Omega} = 1.41$). Key: –, HBM ($n_{\max} = 12$); –○, NS.

upon $n_{\max}$. Therefore, when the super-harmonic responses are of interest, one must carefully select the $n_{\max}$ value. In the primary harmonic response over $0.6 < \overline{\Omega} < 0.8$, the first three harmonics are dominant, as seen from Figs. 6, 7 and 9. For the $n_{\max} = 1$ case, the stiffness transition points are

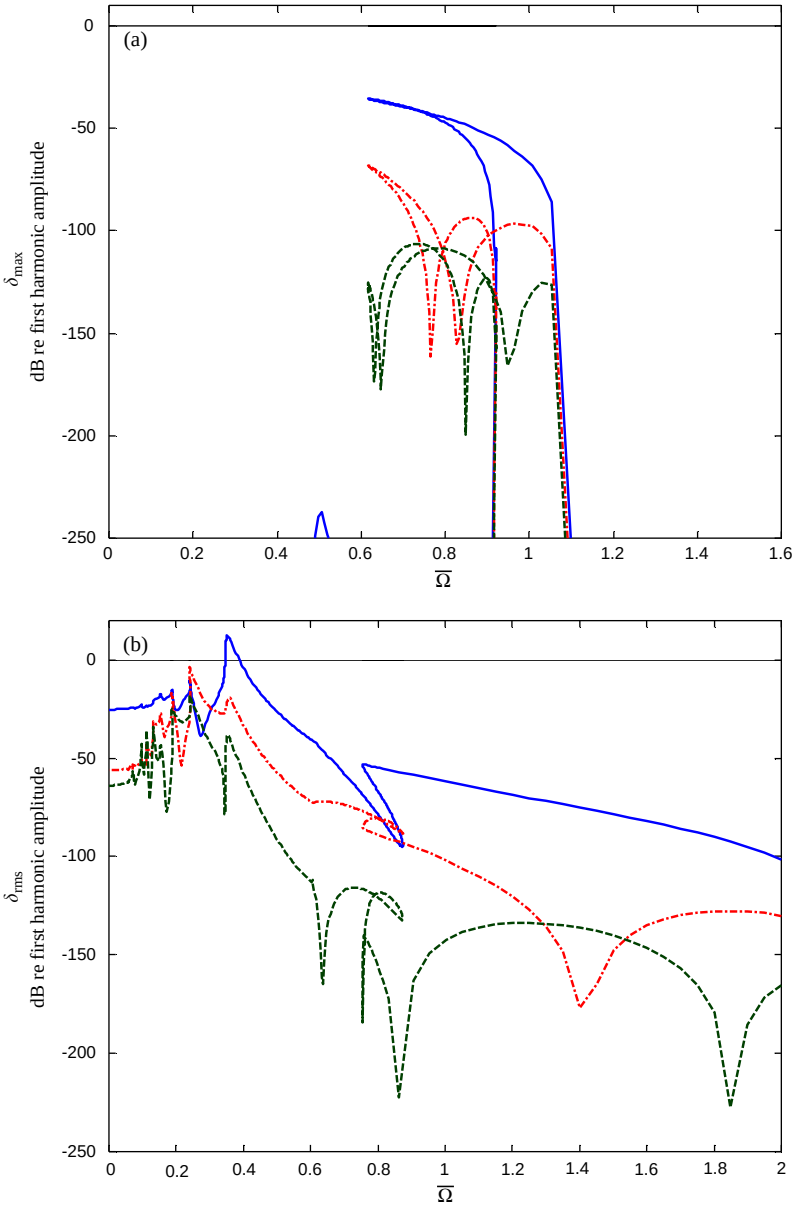

Fig. 11. Relative amplitudes of super-harmonics as predicted HBM. (a) Case 1 with $\alpha = 0.00$; (b) Case 2 with $\alpha = 0.25$. The 0 dB line corresponding to the first harmonic is based on $n_{max} = 12$. Key: –, 2nd harmonic ($n_{max} = 2$); – ·, 3rd harmonic ($n_{max} = 3$); – –, 4th harmonic ($n_{max} = 4$).

significantly different from the $n_{max} = 12$ case. This is because of the asymmetric nature of the nonlinear response. Such an asymmetric response is noticeable in Figs. 6 and 7 when $\alpha \to 0$, and it requires even more harmonics to predict the response. Therefore, one must include at least 3 harmonics especially when $\alpha \approx 0$ as seen in Fig. 11 even for the primary harmonic regime.

6. Appearance of super- and sub-harmonic peaks

Some suggestions about the possible appearance of super- and sub-harmonic responses were introduced by Comparin and Singh [5–7], and Rook and Singh [16–17,21], based mainly on the results yielded by numerical simulations. Essentially when $F_m \leqslant F_p$, there would exist super- and sub-harmonic responses. But, the exact reasons were not clear and therefore we re-examine this issue using the HBM and attempt to find a better prediction scheme [5–7]. Further, some analog simulation (AS) results are also compared with our HBM code for super- and sub-harmonic responses. First, consider the case $F_m = F_p$ when the torque reversal is about to take place. The AS results are based on Comparin and Singh's work [5–7], and their simulated δ_p values are compared with our NS and HBM predictions. The analog simulations were carried out by using a Comdyna GP-6 analog computer where a variable diode function generator was employed to model the clearance nonlinearity [5–7]. Since the analog computer yielded only time-domain signatures, a signal processing procedure was used to transform the results to the frequency domain. Only the mean and standard deviation (which is related to the rms value) of the non-sinusoidal time-domain response were calculated given the sinusoidal excitation. The emphasis of analog simulation was on the prediction of the rms vibration level, and thus a detailed behavior of the actual time histories was not measured [5–7]. Consequently, only limited results from the analog simulations are available for our studies.

In Fig. 12, with $F_m = F_p$, a significant error between analog and digital simulations as well with the HBM is seen over the sub-harmonic response regime ($\overline{\Omega} > 1.0$). Through our analyses, it appears that the only control parameters for the region marked as "E" are the effective inertia (I) and the effective second stage stiffness term (K), as a variation in α or F_p, does not seem to alter the sub-harmonic response. These two parameters (I and K) generate the same results in both NS and HBM. Therefore, the I and K terms used in AS [5–7] must have been different. Results from NS and HBM agree very well even at the sub-harmonic resonant peak, and either method can predict the resonant amplitudes better than the AS. This is due to the fact that the unstable loops around the sub-harmonic ($n\omega_p$) and the fundamental harmonic (ω_p) are not adequately simulated in the AS. The analog simulation appeared to generate only one possible periodic solution when encountering a multi-valued solution regime unlike the HBM. Around the super-harmonic regimes marked as "F", both NS and AS generate only the periodic stable solutions. Therefore, such simulations miss the unstable parts and yield only the amplitudes up to the stable limits of super-harmonic peaks.

The mean operating point δ_m of Fig. 2 migrates back and forth from the second stage of the stiffness to the first stage during the frequency sweep as seen in Fig. 13. Here, mean (δ_m), maximum ($\delta_{\max}$) and minimum ($\delta_{\min}$) values of response are plotted as a function of $\overline{\Omega}$. Physical transition points ($\pm b$ in Fig. 2) are also labeled. In particular, we carefully observe δ_m as and when it crosses the $\pm b$ lines. An appearance of sub-harmonic resonances would depend upon the separation (given by "ℓ"in the dimensionless $\overline{\Omega}$ units) between the primary harmonic of the compliant side (designated as $\overline{\Omega}_{P1}$) and the mean operating point crossover position (given by "G") as presented in Fig. 13. When $\ell \geqslant \overline{\Omega}_{P1}$, a sub-harmonic resonance will appear. As an illustration, consider the $\alpha = 0.25$ case as shown in Fig. 13(a). Here, $\overline{\Omega}_{P1}$ is 0.67 and "G" can be thought to appear at $\ell = \infty$ since δ_m stays only in the first stage. This case clearly demonstrates that a sub-harmonic resonance can be squeezed in around $\overline{\Omega} = 1.34$ that would satisfy $\ell \geqslant \overline{\Omega}_{P1}$.

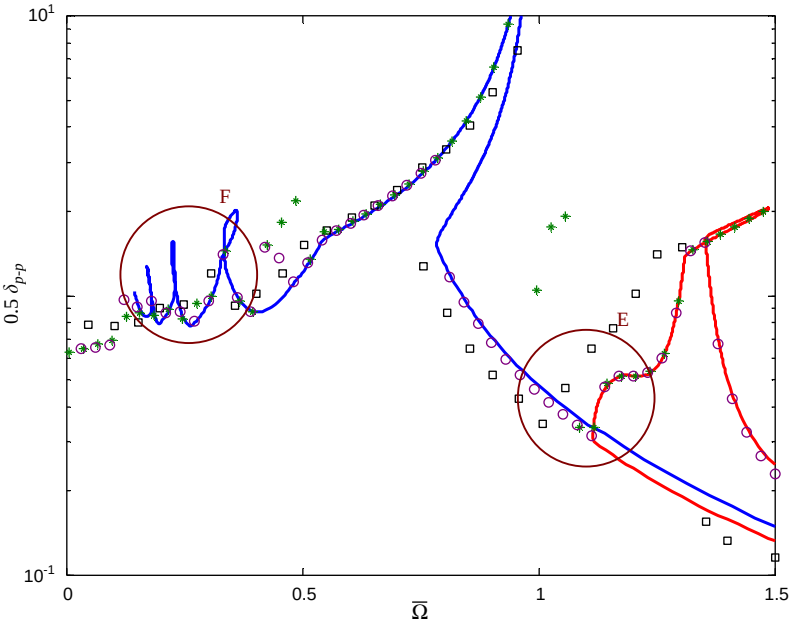

Fig. 12. Comparison between analog computer simulation (AS), numerical simulation (NS) and HBM given $F_m = F_p = 0.25$, $b = 1.0$, $\zeta = 0.015$ and $\alpha = 0.25$. Key: –, HBM ($n_{max} = 12$); □, AS; ○, NSD; ∗, NSU. Analog simulations are from Comparin and Singh [4–7].

Next, we investigate the $\alpha = 0.15$ case where δ_m moves from the second stage to the first at $G = 1.2$. Here, the corresponding $\overline{\Omega}_{P1} = 0.6$ and it also satisfies $\ell \geqslant \overline{\Omega}_{P1}$. An active sub-harmonic response is seen in Fig. 13(b). Conversely, for the case with $\alpha = 0.00$, no sub-harmonic response is observed in Fig. 13(c). This suggests that the α value controls the trajectory of δ_m. For a smaller α, the δ_m migrates more rapidly between the stages (Fig. 13(c)), and ℓ decreases and therefore there is not enough frequency span to squeeze in a sub-harmonic response. In contrast, the δ_m trajectory is smoother when the α value increases to 0.15 or higher as seen in Fig. 13(b).

When the super-harmonic responses appear, their numbers would depend upon the $n_{\max}$ harmonics used in the HBM expansion as discussed before. Further, it is observed that the frequency where the stiffness transitions ($\pm b$) and $\delta_{\min}$ or $\delta_{\max}$ crossover each other plays an important role. The crossover frequency is marked as "H" in Figs. 14 and 15. Some predictions are also listed in Table 4. Active super-harmonic responses are present even when $F_p/F_m \leqslant 1.0$ in contrast with the guidelines suggested by previous researchers [4–7,16–21]. The crossover frequency "H" can be easily calculated by considering the HBM with $n_{\max} = 1$. This is based on the describing function analysis by Comparin and Singh [5–7] where one considers one regime at a time

$$\delta_m = F_m/(f(\delta,\dot{\delta})\omega_1^2), \quad \delta_p = F_p/(-\omega_p^2 + \omega_1^2 f(\delta,\dot{\delta})). \tag{28}$$

Here, the nonlinear function $f(\delta,\dot{\delta})$ and the response δ_p depend upon the δ_m of each super-harmonic, and whether δ_m stays in the first stage or the second stage. The crossover frequency

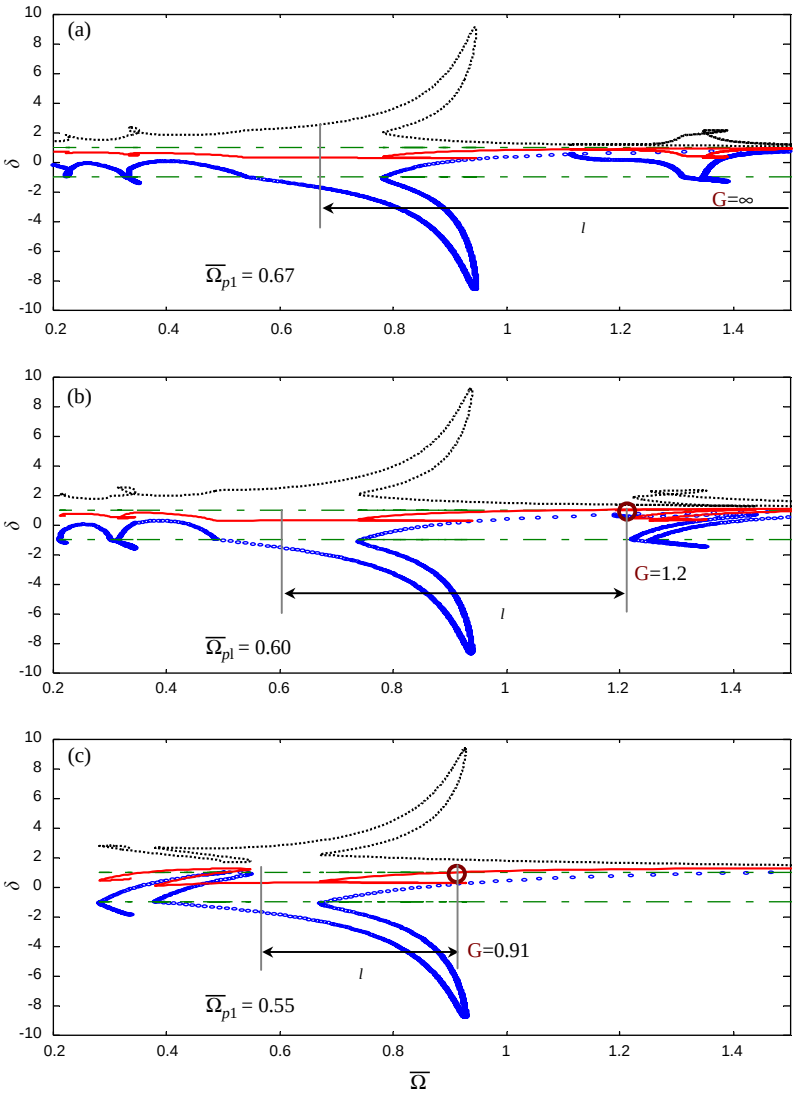

Fig. 13. Sub-harmonic appearances related to the separation ℓ between $\overline{\Omega}_{P1}$ and the crossover frequency "G" given by δ_m and $\pm b$. Given $F_m = F_p = 0.25$, $b = 1.0$, and $\zeta = 0.015$. (a) with $\alpha = 0.25$; (b) with $\alpha = 0.15$; (c) with $\alpha = 0.00$. Key: –, δ_m; · , $\delta_{\max}$; *, $\delta_{\min}$; – · , $\pm b$.

"H" (in the units of $\overline{\Omega}$) can be written as

$$H = \omega_p/\omega_1 = ((\omega_1^2 f - F_p/\delta_p)/\omega_1^2)^{1/2}. \tag{29}$$

Eqs. (28–29) hold only for the no impact and single-sided impact case. Consequently, the HBM with $n_{\max} = 1$ should be used to numerically predict the double-sided impact cases. For the double-sided impacts, the appearance of super-harmonics follows the $F_m \leqslant F_p$ condition that was explained earlier and shown in Figs. 12 and 13. When we consider the single-sided impacts, the following observations can be made. First, consider the case when δ_m starts from the second stage

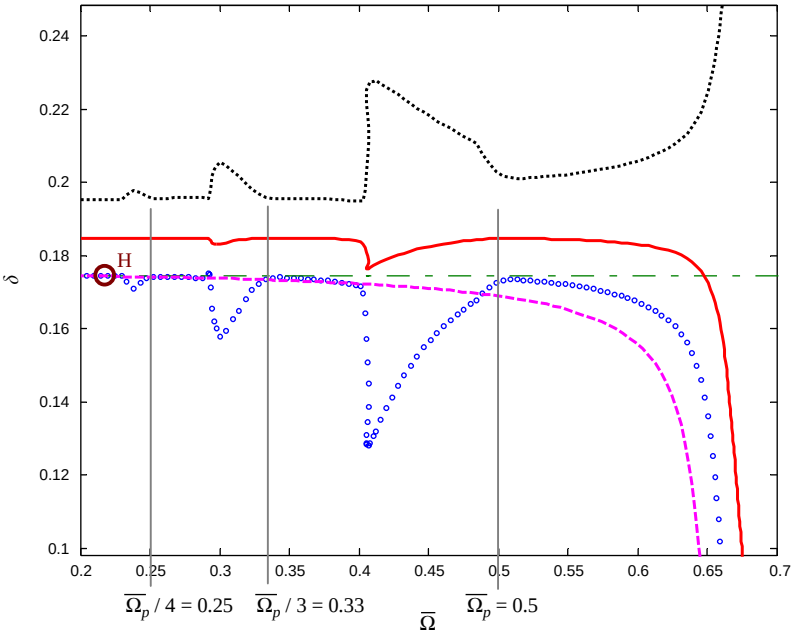

Fig. 14. Super-harmonic appearances and their relationships to the crossover frequency "H" given by b and $\delta_{\min}$. See Table 4 for parameters with $F_m = 0.05$ and $F_p = 0.01$. Key: –, δ_m; ·, $\delta_{\max}$; ○, $\delta_{\min}$ HBM ($n_{\max} = 12$); --, $\delta_{\min}$ prediction (Eqs. (28) and (29) or HBM with $n_{\max} = 1$); – ·, $\pm b$.

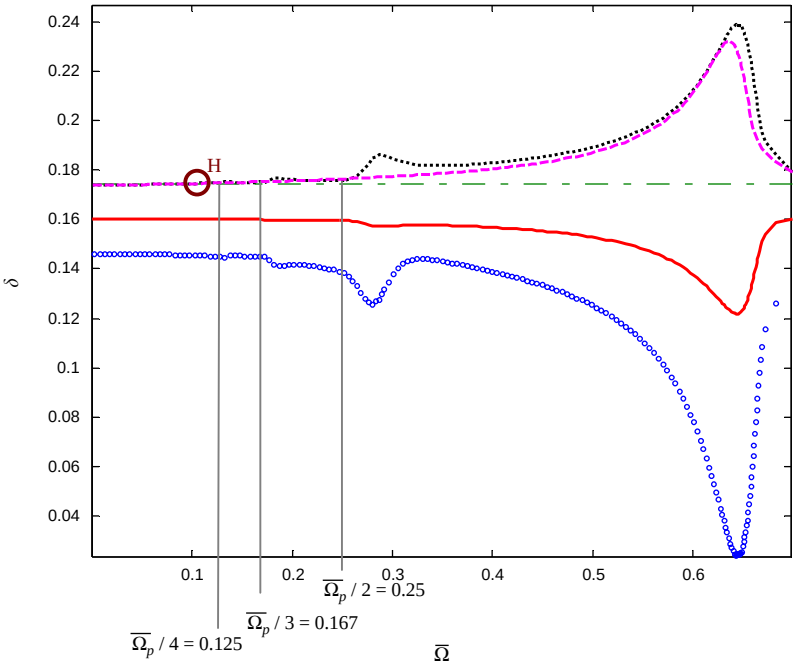

Fig. 15. Super-harmonic appearances and their relationships to the crossover frequency "H" given by b and $\delta_{\min}$. See Table 4 for parameters with $F_m = 0.0035$, and $F_p = 0.04$. Key: –, δ_m; ·, $\delta_{\max}$; ○, $\delta_{\min}$ HBM ($n_{\max} = 12$); --, $\delta_{\max}$ prediction (Eqs. (28) and (29) or HBM with $n_{\max} = 1$); – ·, $\pm b$.

Table 4
Super-harmonic response predictions corresponding to Fig. 14 where $K = 1.0$, $I = 1.0$, $C = 0.05$, $F_p = 0.01$, $b = 10^\circ$, and $\alpha = 0.25$

F_p/F_m	$\overline{\Omega}$ range illustrating possible super-harmonic appearances			
	Theoretical crossover frequency ("H" values)	HBM (with $n_{\max} = 12$)		
		$\overline{\Omega}_P/2 = 0.50$	$\overline{\Omega}_P/3 = 0.33$	$\overline{\Omega}_P/4 = 0.25$
0.200	$\overline{\Omega} > 0.21$	0.51–0.40	0.33–0.29	0.25–0.23
0.185	$\overline{\Omega} > 0.23$	0.51–0.40	0.33–0.29	None observed
0.182	$\overline{\Omega} > 0.36$	0.51–0.40	None observed	None observed
0.172	$\overline{\Omega} > 0.56$	None observed	None observed	None observed

In each case, the softening effect is seen.

as listed in Table 4 and, shown in Fig. 14, the corresponding fundamental harmonic frequency $\overline{\Omega}_p$ is equal to 1. And, the related super-harmonics should appear at $\overline{\Omega}_P/2 = 0.5$, $\overline{\Omega}_P/3 = 0.33$, $\overline{\Omega}_P/4 = 0.25$, and so on. The crossover frequency "H" can be calculated by inserting the $\delta_p = \delta_{\min} = \delta_m - b$ and $f(\delta, \dot{\delta}) = \alpha$ into Eqs. (28) and (29). When "H" resides below one of these super-harmonics, that particular super-harmonic above the "H" value will appear in the nonlinear frequency response curves. Since the impacts for this case dictate a softening type curve, such super-harmonics start from their expected positions and move down in frequencies. For example, the $\overline{\Omega}_P/2$ super-harmonic peak starts from $\overline{\Omega} = 0.5$ but disappears by $\overline{\Omega} = 0.4$, and exhibits a softening-type frequency response shape as observed in Fig. 14. In contrast, when δ_m starts from the first stage of the stiffness, the fundamental frequency $\overline{\Omega}_P$ becomes 0.5. The frequency response now exhibits a stiffening type curve in Fig. 15. And, the super harmonic appearance regimes are given by $\overline{\Omega}_P/2 = 0.25$, $\overline{\Omega}_P/3 = 0.167$, $\overline{\Omega}_P/4 = 0.125$, and so on. Such super-harmonics start from their expected positions and move up in frequency. For example, the $\overline{\Omega}_P/2$ super-harmonic peak starts at $\overline{\Omega} = 0.25$ but disappears by $\overline{\Omega} = 0.32$. In this case, $\delta_p = \delta_{\min} = b - \delta_m$ and $f(\delta, \dot{\delta}) = 1.0$ should be used in Eqs. (28) and (29) for the prediction of "H".

7. Conclusion

This article leads to two distinct but related contributions to the state of art: a new HBM algorithm and a better understanding of the super- and sub-harmonics of a torsional pair with clearance nonlinearity. The validity of a reduced order (sdof) model in capturing the representative behavior of the full torsional system is supported by comparisons to limited experimental results. Reliability of the proposed HBM is shown by comparisons with proven experiments, numerical simulations (NS) and analog simulations (AS). The HBM with adaptive arc-length continuation and stability indication predicts the nonlinear frequency with many advantages. Unlike both analytical and numerical methods, our HBM can find periodic solutions (albeit unstable) in the multi-valued nonlinear regime as well as in possible chaotic or quasi-

periodic response dominated regimes. It requires only $\frac{1}{4}$ of the computational time when compared with the NS.

The effect of the number of harmonics ($n_{\max}$) that could be included in the HBM analysis is clearly visible over the super-harmonic regimes. When active super-harmonic activity is observed, the magnitude differences between $n_{\max} = 1$ and 12 curves approach 10–15 dB, and yet the number of super-harmonic peaks that could be calculated by the HBM code depend strictly upon $n_{\max}$. Although we have considered upto 12 terms, one could choose fewer or more harmonics depending on the problem at hand.

An appearance of the sub-harmonic resonance would depend upon the frequency separation between the primary harmonic of the compliant side and the mean operating point crossover position to the stiffness transitions. Super-harmonic responses are possible even when $F_p/F_m \leqslant 1.0$ although some previous researchers [3–7,16–21] claimed otherwise. It is observed that the frequency, where the stiffness transitions and $\delta_{\min}$ or $\delta_{\max}$ cross over, plays an important role for super-harmonics. Our HBM code provides important clues and suggestions that could lead to a better dynamic design of the torsional systems. Finally, this method will be used to study nonlinear damping mechanisms as well as multi-degree-of-freedom systems with multiple clearances. Future articles would address these issues.

Acknowledgements

This project has been supported by the Gear Rattle Industrial Consortium (Eaton R&D, Spicer Clutch, CRF Fiat, Luk, SAAB and Volvo Trucks) over the 1998–2000 period, and the DaimlerChrysler Challenge Fund since 2000.

References

[1] G.S. Whiston, Impacting under harmonic excitation, *Journal of Sound and Vibration* 67 (1979) 179–186.
[2] T. Sakai, Y. Doi, K. Yamamoto, T. Ogasawara, M. Narita, Theoretical and experimental analysis of rattling noise of automotive gearbox, Society of Automotive Engineers Paper No. 810773 1981, pp. 1–10.
[3] C.N. Bapat, N. Popplewell, K. McLachlan, Stable periodic motions of an impact pair, *Journal of Sound and Vibration* 87 (1983) 19–40.
[4] R. Singh, H. Xie, R.J. Comparin, Analysis of an automotive neutral gear rattle, *Journal of Sound and Vibration* 131 (1989) 177–196.
[5] R.J. Comparin, R. Singh, Nonlinear frequency response characteristics of an impact pair, *Journal of Sound and Vibration* 134 (2) (1989) 259–290.
[6] R.J. Comparin, R. Singh, An analytical study of automotive neutral gear rattle, *Journal of Mechanical Design* 112 (1990) 237–245.
[7] R.J. Comparin, R. Singh, Frequency response of multi-degree of freedom system with clearances, *Journal of Sound and Vibration* 142 (1990) 101–124.
[8] Y.B. Kim, S.T. Noah, Bifurcation analysis for a modified Jeffcott rotor with bearing clearances, *Nonlinear Dynamics* 1 (1990) 221–241.
[9] A. Rust, F. K. Brandl, Definition, identification and elimination of obstructive gear rattle noise, *Proceedings of the XXIII FISITA Congress*, 1990.

[10] Y. Chikatani, A. Suehiro, Reduction of idling rattle noise in trucks, Society of Automotive Engineers Paper No. 911044, 1991, pp. 49–56.
[11] A. Kahraman, R. Singh, Nonlinear dynamics of a geared rotor-bearing system with multiple clearances, *Journal of Sound and Vibration* 144 (1991) 469–506.
[12] M. Kataoka, S. Ohno, T. Sugimoto, A two-degree-of-freedom system including a clearance two-step hardening spring, *Japan Society of Mechanical Engineers, International Journal Series II* 34 (1991) 345–354.
[13] Y.B. Kim, S.T. Noah, Response and bifurcation of a MDOF rotor system with a strong nonlinearity, *Nonlinear Dynamics* 2 (1991) 215–234.
[14] K. Karagiannis, F. Pfeiffer, Theoretical and experimental investigations of gear-rattling, *Nonlinear Dynamics* 2 (1991) 367–387.
[15] F. Pfeiffer, Modeling problems of rattling in gear boxes, *Japan Society of Mechanical Engineers International Conference on Motion and Power Transmissions*, 1991, pp. 43–48.
[16] T.E. Rook, R. Singh, Dynamic analysis of a reverse-idler gear pair with concurrent clearances, *Journal of Sound and Vibration* 182 (2) (1995) 303–322.
[17] C. Padmanabhan, R.C. Barlow, T.E. Rook, R. Singh, Computational issues associated with gear rattle analysis, *Journal of Mechanical Design* 117 (1995) 185–192.
[18] C. Padmanabhan, R. Singh, Dynamics of a piecewise nonlinear system subject to dual harmonic excitation using parametric continuation, *Journal of Sound and Vibration* 184 (5) (1995) 767–799.
[19] E. Trochon, R. Singh, Effects of automotive gearbox temperature on transmission rattle noise, *Noise-Con* 98, 1998, pp. 151–156.
[20] T.C. Kim, R. Singh, Dynamic Interactions between Loaded and Unloaded Gear Pairs under Rattle Conditions, *SAE Transactions, Journal of Passenger Cars: Mechanical Systems* 110 (6) (2001) 1934–1943 (Paper no. 2001-01-1553).
[21] T.C. Kim, T.E. Rook, R. Singh, Effect of smoothening functions on the frequency response of an oscillator with clearance non-linearity, *Journal of Sound and Vibration* 263 (3) (2003) 665–678.
[22] M.A. Veluswami, F.R.E. Crossley, multiple impacts of a ball between two plates-part 1: some experimental observations, *Journal of Engineering for Industry* 19 (1975) 820–827.
[23] R. Shaver, Manual Transmission Clutch Systems, Society of Automotive Engineers, 1997.
[24] J.R. Dormand, P.J. Prince, New Runge–Kutta algorithms for numerical simulation in dynamical astronomy, *Clelstial Mechanics* 18 (1978) 223–232.
[25] C.J. Begley, L.N. Virgin, Impact response and the influence of friction, *Journal of Sound and Vibration* 211 (5) (1998) 801–818.
[26] G. von Groll, D.J. Ewins, The harmonic balance method with arc-length continuation in rotor/stator contact problems, *Journal of Sound and Vibration* 241 (2) (2001) 223–233.
[27] E.L. Allgower, K. Georg, *Numerical Continuation Methods: an Introduction*, Springer, New York, 1990.
[28] P. Sundararajan, S.T. Noah, Dynamics of forced nonlinear systems using shooting/arclength continuation method—application to rotor systems, *Journal of Vibration and Acoustics* 119 (1997) 9–20.
[29] R. Gasch, K. Knothe, *Strukturdynamik II*, Springer, Berlin, 1989.
[30] R. Seydel, *Practical Bifurcation and Stability Analysis*, Springer, Berlin, 1994.
[31] G. Genta, *Vibration of Structures and Machines*, third ed, Springer, Berlin, 1999.
[32] F.H. Ling, X.X. Wu, Fast Galerkin method and its application to determine periodic solutions of nonlinear oscillations, *International Journal of Non-linear Mechanics* 22 (1987) 89–98.
[33] P. Sundararajan, S.T. Noah, An algorithm for response and stability of large order nonlinear systems, application to rotor systems, *Journal of Sound and Vibration* 214 (1998) 695–723.
[34] G. von Groll, D.J. Ewins, On the dynamics of windmilling in aero-engines, *Sixth International Conference on Vibrations in Rotating Machinery*, Institution of Mechanical Engineers, UK, 2000.